

Graph theory-based automated quantum algorithm for efficient querying of acyclic and multiloop causal configurations

**Salvador A. Ochoa-Oregon,^a Juan P. Uribe-Ramírez,^b
Roger J. Hernández-Pinto,^b Selomit Ramírez-Uribe,^b and Germán Rodrigo^a**

^a*Instituto de Física Corpuscular, Universitat de València – Consejo Superior de Investigaciones Científicas, Parc Científic, E-46980 Paterna, Valencia, Spain.*

^b*Facultad de Ciencias Físico-Matemáticas, Universidad Autónoma de Sinaloa, Ciudad Universitaria, CP 80000 Culiacán, Mexico.*

E-mail: salvadorochoa.fcfm@ms.uas.edu.mx,
juanuribe.fcfm@uas.edu.mx, roger@uas.edu.mx,
selomitru@uas.edu.mx, german.rodrigo@csic.es

ABSTRACT: Quantum algorithms provide a promising framework in high-energy physics, in particular, for unraveling the causal configurations of multiloop Feynman diagrams by identifying Feynman propagators with qubits, a challenge analogous to querying *directed acyclic graphs* in graph theory. In this paper, we present the Minimum Clique-optimised quantum Algorithm (MCA), an automated quantum algorithm designed to efficiently query the causal structures within the Loop-Tree Duality. The MCA quantum algorithm is optimised by exploiting graph theory techniques, specifically, by analogy with the Minimum Clique Partition problem. The evaluation of the MCA quantum algorithm is exhibited by analysing the transpiled quantum circuit depth and quantum circuit area.

Contents

1	Introduction and motivation	1
2	Causality from the loop-tree duality	3
3	Quantum algorithms for querying causality of multiloop graphs	4
3.1	Boolean construction of eloop clauses	5
3.2	Quantum registers	6
4	The Minimum Clique-optimised quantum algorithm	8
4.1	Graphs as data structures and search of clique	8
4.2	Ancillary qubits optimisation	9
4.3	Oracle construction automation	11
5	Aplication of the MCA quantum algorithm to multiloop topologies with four and five eloops	13
5.1	Four eloops with contact interaction	14
5.2	The t channel at four eloops	15
5.3	The u –channel at four eloops	16
5.4	Five eloops with contact interaction	16
6	Transpilation behaviour	17
7	Conclusions	21
A	Clauses of multiloop topologies: four and five eloops	26
A.1	Four eloops with contact interaction	26
A.2	Four eloops: s – and t –channels	26
A.3	Four eloops: u channel	27
A.4	Five eloops with contact interaction	27
B	Algorithms	28

1 Introduction and motivation

The description of the fundamental interactions of elementary particles in High-Energy Physics (HEP) requires a deep understanding of Quantum Field Theory (QFT). Large-scale collider experiments, most notably the CERN’s Large Hadron Collider (LHC), are devoted

to rigorously testing the predictions of the Standard Model (SM) with unprecedented accuracy, in the ongoing quest for signals of new physics beyond the current theoretical framework. In order to gain a meaningful and decisive insight into the properties of the fundamental interactions, it is important to contrast experimental data with theoretical predictions of the highest achievable precision. For instance, the Higgs boson discovered in 2012 [1, 2] caught the attention of phenomenologist leading to the first calculations up the Next-to-Next-to-Leading Order ($N^2\text{LO}$) in the strong coupling for the $H \rightarrow \gamma\gamma$ process; nowadays, it is known the Next-to-Next-to-Next-to-Leading order ($N^3\text{LO}$) in QCD with the aim of increasing the accuracy for the future colliders [3–8]. These tasks involve addressing the central bottlenecks of theoretical high-energy physics in dealing with quantum fluctuations at higher orders in the perturbative expansion. Despite the progress and the various efficient strategies developed so far [9], achieving the theoretical precision required at high-energy colliders calls for exploring approaches that surpass the current state of the art and drive further progress towards higher perturbative orders.

To address this challenge, quantum computing represents a promising approach in HEP [10–12], opening new paradigms for solving different types of problems where the quantum principles of entanglement and superposition can provide an advantage over classical methods. In the framework of the Loop-Tree Duality (LTD), the inherent relation between causality in multiloop Feynman diagrams and directed acyclic graphs (DAGs) in graph theory, has motivated the development of various quantum algorithms for causal querying [13–15].

The relevance of the LTD framework is founded on the intrinsic property of providing more stable integrands [16, 17] by manifestly cancelling all non-causal singularities. Furthermore, it has been recently shown that the computation of vacuum amplitudes in LTD gives rise to integrand representations of physical observables that are well-defined directly in the four physical dimensions of the spacetime [18, 19]. Therefore, casting all causal configurations of a multiloop vacuum diagram is crucial to disentangle the physics of elementary particles in QFT calculations. In this paper, we present a novel quantum algorithm for the querying of causal structures, dubbed Minimum Clique-optimised quantum Algorithm (MCA), which is based on the Minimum Clique Partition (MCP) [20] problem in graph theory. In particular, we focus on automating the process of constructing the oracle operator and optimising the transpiled quantum circuit of the proposed quantum algorithm.

This document is organized as follows: in Sec. 2, we briefly introduce the ideas of causality in LTD; in Sec. 3, we present the principal components of Grover’s based quantum algorithms and its relations to DAGs; in Sec. 4, we introduce the MCA quantum algorithm and analyse different strategies for optimisation and automation of the quantum querying oracle; in Sec. 5, we present the implementation of the proposed quantum algorithm to new topologies at four and five loops, demonstrating how efficiently these are tackled with our methodology; in Sec. 6, we present a transpilation analysis of the MCA quantum algorithm, and contrast it with the results of the MCX quantum algorithm [15]; and finally, in Sec. 7 we present the conclusions and outline the perspectives of the work.

2 Causality from the loop-tree duality

The computation of high-precision theoretical predictions for observables in HEP relies on the manipulation of scattering amplitudes at high perturbative orders in QFT. It is well known that these theoretical predictions are extracted after the cancelation of different divergences. The methodology for removing the divergences from singular configurations at high energy depends on the renormalization procedure, while soft and collinear configurations require the construction of suitable counterterms. One of the potential bottlenecks is the proliferation of non-causal or non-physical divergences in loop Feynman diagrams. In this direction, LTD [21–40] has made significant progress by enabling the manifest cancellation of such non-physical singularities at the integrand level. This is achieved by exploiting the causal structure of scattering and vacuum amplitudes.

Feynman propagators encode the information on the particle propagation between two interaction vertices in either direction, i.e. positive and negative energy modes. Explicitly, a Feynman propagator is given by,

$$G_F(q_i) = \frac{1}{\left(q_{i,0} + q_{i,0}^{(+)}\right) \left(q_{i,0} - q_{i,0}^{(+)}\right)}, \quad (2.1)$$

with $q_{i,0}$ the energy component of the four momenta q_i , $q_{i,0}^{(+)} = \sqrt{\vec{q}_i^2 + m_i^2 - \imath 0}$ the on-shell energy, and $\imath 0$ the customary Feynman complex prescription. Thus, a loop Feynman diagram contains configurations where a particle departs from an interaction vertex and returns to the initial point, traveling back in time and therefore breaking causality. A key consequence of it is that certain singular configurations are related with non-causal processes, which are costly computationally and numerically unstable. On the other hand, causal configurations are equivalent to DAGs in terms of graph theory, due to the fact that only the forward direction in time is allowed when the energy flux of a Feynman diagram is concerned. It has been demonstrated that the LTD representation of a scattering amplitude involves the causal configurations only. Therefore *any observable in LTD is written in such a way that causality is manifestly preserved*. In the following, we provide the basic ideas behind the LTD and its connection with DAG configurations in graph theory [16, 17, 41–49].

In LTD, a scattering amplitude in d spacetime dimensions is written as,

$$\mathcal{A}^{(\Lambda)} = \int_{\vec{\ell}_1 \dots \vec{\ell}_\Lambda} \mathcal{A}_D^{(\Lambda)}, \quad (2.2)$$

with

$$\int_{\vec{\ell}_j} = \mu^{4-d} \int \frac{d^{d-1} \vec{\ell}_j}{(2\pi)^{d-1}}, \quad (2.3)$$

where Λ is the number of independent loop momenta, and the integrand $\mathcal{A}_D^{(\Lambda)}$ is the dual amplitude, which is a function of the loop and external three-momenta. The energy scale μ

is arbitrary. For vacuum amplitudes, the integrand contains only causal propagators of the form

$$\frac{1}{\lambda_{i_1 i_2 \dots i_n}} = \frac{1}{\sum_{s=1}^n q_{i_s,0}^{(+)}}. \quad (2.4)$$

As the topological complexity of a vacuum diagram increases, the number of possible causal propagators grows rapidly, as well as the number of combinatorial combinations of causally compatible or causally entangled causal propagators.

Quantum computing algorithms excel in problems of increasing complexity that inherently leverage quantum superposition. A property perfectly exemplified by a Feynman propagator, when interpreted as the quantum superposition of two distinct energy modes. Thus, we can incorporate the ideas of causality, by formally defining a Feynman propagator in terms a superposition of quantum mechanical states,

$$G_F(q_i) \equiv \frac{1}{\sqrt{2}}(|0\rangle + |1\rangle), \quad (2.5)$$

with $|0\rangle$ and $|1\rangle$ the positive and negative energy modes, respectively. This notation shall be useful for describing DAGs in the quantum querying algorithm.

3 Quantum algorithms for querying causality of multiloop graphs

The quantum causal query algorithms presented in Refs. [13, 15], relating causality of multiloop Feynman diagrams with DAGs, are based on three fundamental concepts: *i*) the bootstrapping of the LTD causal representation based on *reduced* equivalent graphs built from vertices and edges [44, 45], *ii*) the design of a quantum oracle capable of identifying acyclic configurations with minimal quantum resources and *iii*) the strategies that enable an efficient amplitude amplification.

Under the assumption of a description with reduced graphs, an edge is defined as the union of multiple Feynman propagators connecting two interaction vertices. After the propagators are merged into edges, the loops associated to the reduced graph are called eloops. Reliance on this framework is well justified, as causal configurations are only those in which the momentum flows of all propagators belonging to each edge, are aligned in the same direction. In addition, considering eloops simplifies the analysis of causal conditions by reducing the number of acyclic configurations to identify.

A quantum query algorithm based on Grover's algorithm [50] consists of the following stages: *i*) encoding the edge information in qubits, *ii*) initializing each qubit in the quantum circuit, *iii*) designing an oracle operator to tag acyclic states, *iv*) applying a diffusion operator to implement amplitude amplification and *v*) measuring the resulting quantum state. It is important to remark that the efficiency of the query algorithms critically relies on the design of the oracle operator. Therefore, the aim of proposing a new quantum algorithm

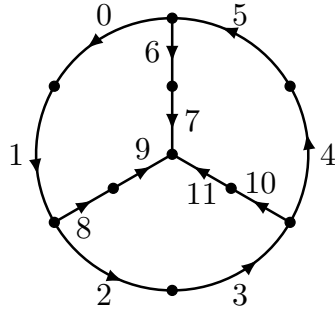


Figure 1: A three-eloop topology with two edges per set. The edges are labeled considering the short hand notation $i \equiv e_i$ and the direction of the arrows represent the $|1\rangle$ states. External particles that may be attached to the vertices are not shown.

is to achieve an optimal and automated oracle operator design, which efficiently encodes all causal conditions in a streamlined form.

In order to optimise the quantum circuit, we focus on reducing the number of qubits required by exploiting the property of mutually exclusive clauses. This property allows information from different control qubits to be stored in a common target qubit. In the context of automating the algorithm, we explore the use of graph features as a data structure to search for mutually exclusive clauses, and also apply them to the efficient design of the oracle operator.

To evaluate the efficiency of the proposed MCA quantum algorithm, we analyse the number of qubits needed for the algorithm implementation, the theoretical quantum circuit depth and the transpiled quantum circuit area. Before delving into the description of the MCA quantum algorithm, we review the concepts related to the Boolean construction of the causal clauses and describe the quantum circuit components.

3.1 Boolean construction of eloop clauses

The identification of causal configurations is approached by suppressing the cyclic configurations. The directed cyclic conditions are stored in eloop clauses, which are defined by a specific set of edges. We introduce z_j as the set of indices associated to the edges depending on the same linear combination of loop momenta. Given the set z_j we define the following Boolean functions,

$$s_j \equiv \bigwedge_{i \in z_j} e_i, \quad \text{and} \quad \bar{s}_j \equiv \bigwedge_{i \in z_j} \bar{e}_i, \quad (3.1)$$

where e_i represents the state of edge i , the Boolean function s_j is defined with the AND operator, \wedge , and \bar{s}_j represents the Boolean function with the mirror states of the edges within the specified set. The total number of edges constituting a multiloop topology is given by $n = \sum_j n_{s_j}$, where n_{s_j} denotes the total number of edges in the set z_j . For

example, for the three-eloop topology depicted in Fig. 1,

$$\begin{aligned} s_0 &= e_0 \wedge e_1, & s_1 &= e_2 \wedge e_3, & s_2 &= e_4 \wedge e_5, \\ s_3 &= e_6 \wedge e_7, & s_4 &= e_8 \wedge e_9, & s_5 &= e_{10} \wedge e_{11}. \end{aligned} \quad (3.2)$$

Relying on Eq. (3.1) enables to simplify the encoding of the eloop clauses, in such a way that they still depend on the number of sub-eloops but not longer on the number of propagators. The maximal number of eloop clauses is determined by the total number of directed cyclic configurations, $m = 2\ell$, where ℓ denotes the total number of sub-eloops. The eloop-clause conditions are given by

$$c_k \equiv \bigwedge_{j \in S_k} s_j, \quad c_{\ell+k} \equiv \bar{c}_k \quad \text{with} \quad k = 0, \dots, \ell - 1, \quad (3.3)$$

where capital S_k denotes the set of edges generating the cyclic configuration contained in the sub-eloop k . Back to the three-eloop example, there are three sub-eloops involving three sets of edges and four sub-eloops involving four sets of edges, therefore the maximal number of eloop clauses is fourteen. Explicitly,

$$\begin{aligned} c_0 &= s_0 \wedge s_1 \wedge s_2, & c_1 &= s_0 \wedge \bar{s}_3 \wedge s_4, & c_2 &= s_1 \wedge \bar{s}_4 \wedge s_5, \\ c_3 &= s_2 \wedge s_3 \wedge \bar{s}_5, & c_4 &= s_0 \wedge s_1 \wedge \bar{s}_3 \wedge s_5, & c_5 &= s_1 \wedge s_2 \wedge s_3 \wedge \bar{s}_4, \\ c_6 &= s_0 \wedge s_2 \wedge s_4 \wedge \bar{s}_5, & c_{7+k} &= \bar{c}_k, \end{aligned} \quad (3.4)$$

with $k = 0, \dots, 6$. Once the eloop clauses c_k are established, the set of acyclic configurations is composed by those fulfilling the following Boolean condition

$$\mathcal{A} \equiv \bigwedge_j \neg c_j. \quad (3.5)$$

The representation of eloop clauses through Boolean functions is motivated from the fact that, at the quantum circuit level, the Boolean operator \wedge is associated with a multicontrolled Toffoli gate [15].

3.2 Quantum registers

Grover's quantum algorithm aims to query a specific number of r winning states over a total number of $N = 2^n$ states, with n the number of qubits generating all the possible states. The mixing angle, $\theta = \arcsin(\sqrt{r/N})$, measures the ratio between the number of winning states and the total number of states, specifically, the condition given by $\theta \lesssim \pi/6$ ($r/N \lesssim 1/4$) determines the applicability of Grover's quantum algorithm. In addition, the mixing angle θ determines the number of iterations, t , that the oracle and diffuser operators should be applied. The optimal value of t is obtained when $\sin^2 \theta_t \sim 1$, with $\theta_t = (2t + 1)\theta$, particularly $t = 1$ is achieved when $\theta \sim \pi/6$ equivalent to $r/N \sim 1/4$.

The multiloop topologies that we consider in the analysis are those included in the classification scheme of multiloop topologies provided in Refs. [17, 41, 51] allowing to

describe any scattering amplitude up to five loops. From a classical and quantum approach, it has been shown [15] that the number of causal configurations is typically about one half of the total number of possible configurations, which is not optimal for amplitude amplification. In order to circumvent this limitation it is required to reduce the ratio between the number of configurations to query and the total number of possible configurations. The two strategies to achieve an optimal amplitude amplification are either to halve the number of causal configurations to query by tagging the state of one edge, or to increase the total number of possible states by introducing additional qubits.

To fix an edge direction, we leverage the symmetry inherent to all diagrams, which satisfy the property that when a causal solution is provided, its mirrored state with all momentum flows reversed is also a causal solution. It is important to highlight that this property also reduces the number of Boolean clauses necessary for the construction of the oracle. If this modification is not sufficient to obtain a proper value of r/N , we increase the value of N by adding an ancillary qubit. This adjustment is reserved as a last option, as increasing the number of qubits also increases the quantum circuit depth.

Recapping the example of three-eloop topology with two edges per set, we have that $r/N \sim 1/2$. So, we tag the state of one edge, adopting as a convention the edge e_0 . Reformulating and relabeling the indices of the eloop clauses shown in Eq. (3.4) results in a reduction from fourteen to ten clauses:

$$\begin{aligned} c_0 &= s_0 \wedge s_1 \wedge s_2 , & c_1 &= s_0 \wedge \bar{s}_3 \wedge s_4 , & c_2 &= s_1 \wedge \bar{s}_4 \wedge s_5 , \\ c_3 &= s_2 \wedge s_3 \wedge \bar{s}_5 , & c_4 &= s_0 \wedge s_1 \wedge \bar{s}_3 \wedge s_5 , & c_5 &= s_1 \wedge s_2 \wedge s_3 \wedge \bar{s}_4 , \\ c_6 &= s_0 \wedge s_2 \wedge s_4 \wedge \bar{s}_5 , & c_7 &= \bar{c}_2 , & c_8 &= \bar{c}_3 , & c_9 &= \bar{c}_5 . \end{aligned} \quad (3.6)$$

The implementation of the MCA quantum algorithm requires three different classes of qubit registers. The first register, denoted by $|e\rangle$, is responsible of encoding the two possible states of the edges defining the multiloop topology. The second register is denoted by $|a\rangle$ and is composed by *ancillary qubits* which store the causal eloop clauses. The last register encodes the oracle marker, $|out\rangle$, which distinguishes whether the graph configuration corresponds to a causal solution or not. The $|e\rangle$ register is initialised in a uniform superposition by applying Hadamard gates to the n qubits characterizing the edges, $|e\rangle = H^{\otimes n}|0\rangle$; in the case of the $|a\rangle$ register, the m ancillary qubits are initialised to the $|1\rangle$ state through the application of XNOT gates, $|a\rangle = X^{\otimes m}|0\rangle$; and the oracle marker is initialised to the Bell state $|-\rangle$ by $|out\rangle = |-\rangle = H(X|0\rangle)$.

Once the initialisation of all registers has been completed, the oracle operator encoding all eloop clauses is applied through the phase kick-back property,

$$U_w|e\rangle|a\rangle|out\rangle = (-1)^{f(a,e)}|e\rangle|a\rangle|out\rangle , \quad (3.7)$$

where $f(a, e) = (\wedge_i a_i) \wedge e_0$, and e_0 is the edge whose state is tagged. Before moving forward to the probability amplification by the diffuser operator, the oracle operator is applied in reverse order to restore each qubit in its initial state, with the exception of $|out\rangle$. Once this

point is reached, the diffusion operator, U_s , is applied to the $|e\rangle$ register. In this work, the diffusion operator used is the one described in the PennyLane documentation [52].

The following section shows in detail the design of the oracle operator, taking into account the impact of the number of eloop clauses in the required computational resources.

4 The Minimum Clique-optimised quantum algorithm

The effectiveness of quantum query algorithms based on amplitude amplification critically relies on the oracle operator design. The eloop clauses required to construct the oracle operator are established according to the diagram complexity scaling polynomially. Therefore, it is important to have in mind that a larger number of clauses implies a higher resource consumption either in the number of qubits, the number of quantum gates needed, or the quantum depth of the quantum circuit.

In this section we present the MCA approach to optimise the number of eloop clauses and quantum gates needed, as well as an automated procedure to apply them. The MCA quantum algorithm uses fundamental graph theory concepts to process the graph structure more efficiently, with the aim of having a positive impact on reducing the number of qubits required in the eloop-clause quantum register $|a\rangle$. Furthermore, this reduction results in lowering the theoretical quantum depth of the quantum circuit, which has a direct impact on reducing the expected quantum noise in quantum hardware.

4.1 Graphs as data structures and search of clique

Graph theory has become an important mathematical tool in a wide variety of applications. Particularly in computer science, graphs have emerged as a fundamental data structure [53] for modelling relationships between pairs of objects. One of the most interesting features of this data structure is its inherent ability to represent multiple relationships between objects, which categorizes it as a non-linear data structure. This nonlinearity has allowed the development of algorithms capable of solving a diverse range of problems [54].

A fundamental concept used to design and automate the MCA quantum algorithm is the identification of cliques in an undirected graph. A clique, also known as a complete subgraph, is defined as a subset of vertices from a specific graph in which each pair of vertices is directly connected by an edge. For example, the graph depicted in Fig. 2 contains a clique composed by the set of vertices $\{A, B, C\}$. In particular, we focus on determining the minimum number of cliques that generate a graph, a problem known as Minimum Clique Partition (MCP) [20]. To clarify the idea behind the MCP problem, we recall the graph shown in Fig. 2, which MCP solution is given by the configuration of the clique generated by the set of vertices $\{A, B, C\}$ and the clique formed solely by the vertex D .

The advantage of associating eloop clauses with a subgroup of vertices defining a graph, and characterizing the corresponding edges with the desired criteria, is that an eloop clause optimisation problem can be treated as a MCP problem of the corresponding graph.

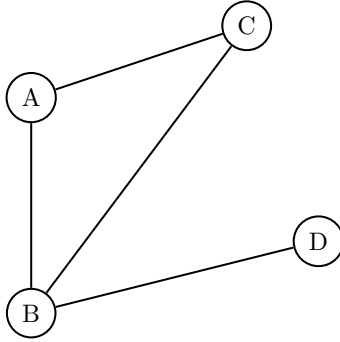


Figure 2: Graph consisting of vertices A, B, C and D, with a clique composed by the set of vertices $\{A, B, C\}$.

It is also important to note that the MCP problem is NP-hard [55], which means that a fully general solution to this problem is beyond the scope of this work. Nevertheless, we provide an approximate solution that has proven to be suitable for our purposes.

4.2 Ancillary qubits optimisation

The idea behind the MCA quantum algorithm to optimise the number of ancillary qubits for the encoding of the eloop clauses is based on the concept of “mutually exclusive clauses”, i.e., clauses that cannot be satisfied simultaneously for a given diagram configuration. An example of mutually exclusive clauses is the pair of clauses c_2 and c_7 of Eq. (3.6), declaring one of them true automatically implies that the other clause is false. It is important to note that by associating the concept of mutually exclusive clauses with a truth table, it is possible to establish the equivalence of mutually exclusive clauses with the Boolean XOR operator (\vee).

A useful relationship among the operators OR, AND and XOR is given by

$$c_i \vee c_j = (c_i \vee c_j) \vee (c_i \wedge c_j) , \quad \forall i, j . \quad (4.1)$$

If $c_i \wedge c_j = \emptyset$, it is said that c_i and c_j ($i \neq j$) are mutually exclusive clauses and Eq. (4.1) simplifies to

$$c_i \vee c_j = c_i \vee c_j , \quad \forall i \neq j . \quad (4.2)$$

At the quantum circuit level, the condition given by Eq. (4.2) indicates the feasibility to store the information of both clauses in a single qubit. The identification of mutually exclusive clauses allows a significant reduction in the number of required ancillary qubits.

The problem of optimising the number of ancillary qubits can be treated as the search of the smallest number of mutually exclusive subset clauses. The relation between clauses is illustrated through a graph, where a mutually exclusive clause set is represented with a clique. In order to address the problem in the realm of graph theory, we construct the adjacency matrix, which describes the space of eloop clauses. The **Algorithm 1** (B1),

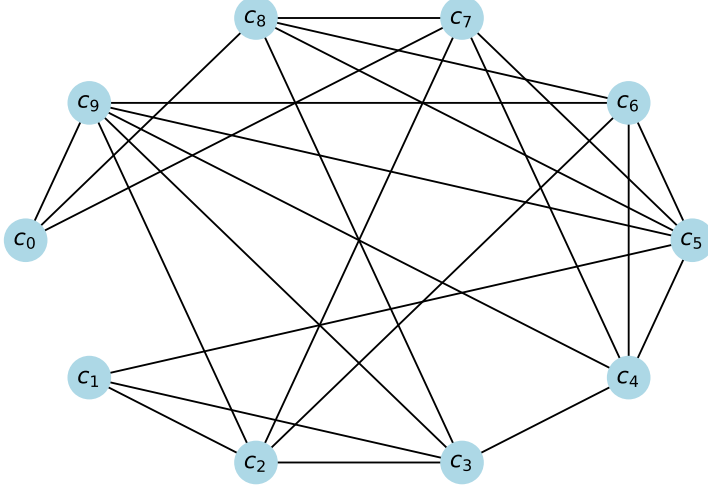


Figure 3: Graph representing the adjacency matrix of the three-loop topology with two edges per set (Fig. 1).

called `MutualAuxMatrix`, constructs a matrix whose entries are composed by zeros and ones; if the entry is one, the pair of clauses satisfies Eq. (4.2), otherwise the entry is zero.

The graph associated to the generated adjacency matrix is a practical tool to visualise the existence of multiple combinations of mutually exclusive clauses. Recalling the three-loop topology with two edges per set, Fig. 3 shows the corresponding graph of the adjacency matrix generated with the clauses in Eq. (3.6). In order to find the minimum number of cliques in a graph, the **Algorithm 2** (B2) called `GraphConditionCombination` has been developed. This algorithm uses the function `find_cliques`¹ from `Networkx` library [57] which obtains all cliques in the provided adjacency matrix. The key is to identify the *maximum clique*, the clique containing the highest number of clauses.

Once the maximum clique has been selected, the corresponding combination of clauses is stored and the associated nodes are removed from the graph. This process is equivalent to delete the rows and columns corresponding to each clause in the adjacency matrix, and is repeated until all the nodes of the graph are removed. The output consists of a set of mutually exclusive subsets of clauses; in terms of the quantum circuit it defines a set of Mutual Auxiliary clauses (MAUX_C). It is important to mention that the `GraphConditionCombination` algorithm depends only on the structure of the graph, therefore, it becomes an important tool to automate the design of the set gates associated to the oracle operator.

The application of **Algorithm 2** to the adjacency matrix associated to Fig. 3 yields the following sets:

$$\text{MAUX}_C^{(3,12)} = \{\{c_4, c_5, \bar{c}_5, c_6\}, \{c_0, \bar{c}_2, \bar{c}_3\}, \{c_1, c_2, c_3\}\}, \quad (4.3)$$

¹This function is based on the algorithm described in Ref. [56]

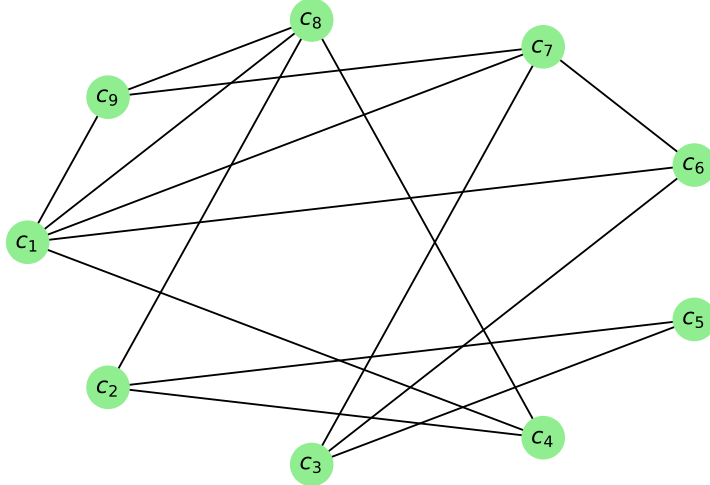


Figure 4: Graph of mutually exclusive clauses for the three-eloop topology with two edges per set shown in Fig. 1.

where the superindex, (ℓ, e) , indicates the number of eloops and the number of edges respectively. In this example, the number of required ancillary qubits is three, each one corresponding to each set in $\text{MAUX}_C^{(3,12)}$. This number represents a reduction of $\mathcal{O}(57\%)$ in the number of ancillary qubits compared to the seven ancillary qubits required with the MCX algorithm [15]. It is important to highlight that the advantage of encoding eloop clauses through multicontrolled Toffoli gates is that the result obtained in Eq. (4.3) remains unchanged even if the number of propagators per set increases.

4.3 Oracle construction automation

The design of the oracle operator requires to identify the eloop clauses encoding the causal conditions, and to define the order in which the eloop clauses are applied. The eloop clauses are implemented through multicontrolled Toffoli gates and XNOT gates, where the XNOT gates play the role of generating the states \bar{s}_j . The order in which the gates are applied directly impacts the quantum depth of the quantum circuit. In this section we present an automated optimisation process to reduce the quantum depth by defining the more efficient order to apply the eloop clauses.

The central idea is to group the eloop clauses in the diagram into sets. As a first stage, we cluster the clauses that have no common edges; the second stage considers the remaining eloop clauses of the diagram which satisfy the condition that they match at least one state s_j or \bar{s}_j . Explicitly, these two stages can be related only by Boolean conditions s_k and \bar{s}_k for some k such that if $s_k \in c_i$ and $\bar{s}_k \in c_j$, then

$$s_k \in c_i \cap \bar{c}_j. \quad (4.4)$$

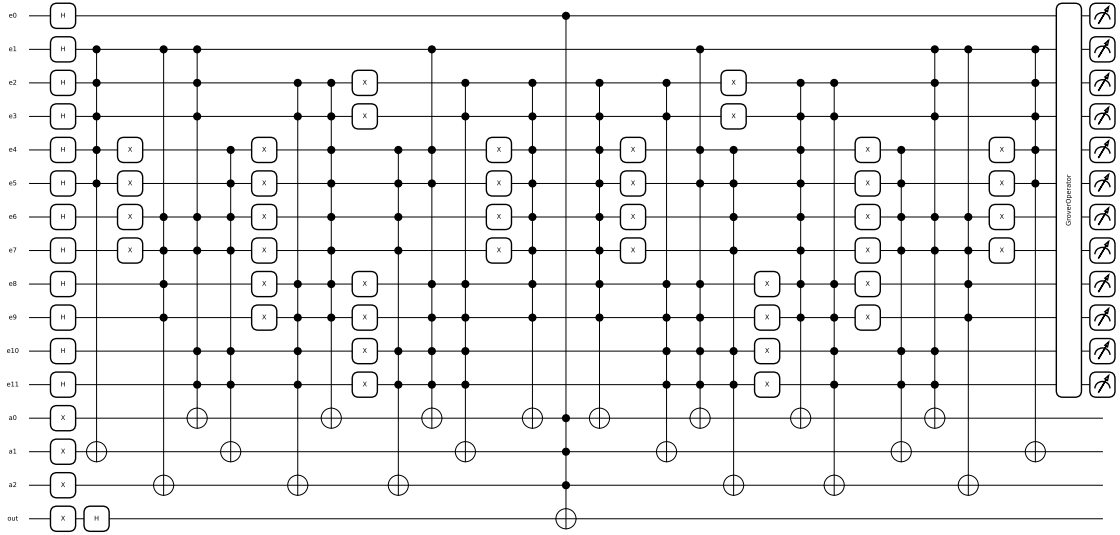


Figure 5: Quantum circuit associated for the three-eloop topology with two edges per line shown in Fig. 1.

At quantum circuit level, the condition in Eq. (4.4) allows to apply a single column of XNOT gates, which prepares the corresponding states for all the clauses belonging to the set, followed by applying the corresponding multicontrolled Toffoli gates. In the third stage, the clause corresponding to the condition of the outer edges of the diagram is taken as an independent set, given the fact that including XNOT gates it is not necessary to prepare the states of this clause.

The adjacency matrix associated to the eloop clauses must satisfy the three stages described above, and through the `GraphConditionCombination` algorithm the possible set combinations are reduced. The advantage of this oracle design is that with the first stage we enable multiple eloop clauses to be applied in a single time step, and with the second stage we prevent an additional contribution to the quantum depth value by applying a single column of XNOT gates.

Following the three-eloop example, Fig. 4 shows a representative graph of the adjacency matrix obtained with the `MutualClausesMatrix` algorithm to the eloop clauses in Eq. (3.6). The application of the `GraphConditionCombination` algorithm to Fig. 4 generates the following sets of Mutual clauses (`MUTC`):

$$\text{MUT}_C^{(3,12)} = \{\{c_0\}, \{c_1, c_4, \bar{c}_3\}, \{c_3, c_6, \bar{c}_2\}, \{c_2, c_5\}, \{\bar{c}_5\}\} . \quad (4.5)$$

Once the `MUTC` set has been obtained, the oracle operator is implemented through the clause blocks given in Eq. (4.5). In this case, the maximum theoretical quantum circuit depth is twenty-nine.

It is important to highlight that the order of the sets contained in `MUTC` is not unique, therefore, the quantum circuit depth varies for each one of them. This scenario presents

notable similarities to the process of identifying the optimal set of hyperparameters to maximise or minimise a specific metric for machine learning models. Specifically, we minimise the quantum circuit depth by generating an optimally ordered MUT_C set (OMUT_C) applying Optuna [58], a library widely used for hyperparameter optimization of large deep learning models. Optuna is based in the Tree-structured Parzen Estimator algorithm (TPE) [59], which is a Bayesian optimization algorithm that trains two Gaussian Mixture Models, one to the set of parameter values associated with the best objective values which is commonly denoted by $l(x)$, and another to the remaining parameter values, denoted by $g(x)$. From these two models it chooses the parameter value x that maximizes the ratio $l(x)/g(x)$ and like a tree, performs a cut-off at this value of x which provides the set of hyperparameter values to evaluate.

Applying this procedure to the set $\text{MUT}_C^{(3,12)}$ in Eq. (4.5) we obtain

$$\text{OMUT}_C^{(3,12)} = \{\{c_0\}, \{c_1, c_4, \bar{c}_3\}, \{c_2, c_5\}, \{c_3, c_6, \bar{c}_2\}, \{\bar{c}_5\}\}. \quad (4.6)$$

Implementing the oracle operator using the optimized ordering of the clause blocks obtained in Eq. (4.6) reduces the theoretical quantum circuit depth from twenty-nine to twenty-three. Gathering the steps described in this section provides the complete procedure of the MCA quantum algorithm. Particularly, the quantum circuit for the three-eloop topology in Fig. 1 is shown in Fig. 5.

The three-eloop topology with twelve edges presented in this section, has been used as an illustrative example of the application of the MCA quantum algorithm. The sets contained in MAUX_C in Eq. (3.6) represent the smallest set of eloop clauses for the most general three-eloop topology. Regarding the structure of the oracle operator through the eloop clauses in MAUX_C , the MUT_C sets given in Eq. (4.5) provide the most convenient clustering, whereas the sequence of sets in OMUT_C shown in Eq. (4.6) introduces an optimal ordering of the eloop clauses, thereby reducing the quantum circuit depth.

5 Application of the MCA quantum algorithm to multiloop topologies with four and five eloops

The procedure to obtain MAUX_C and OMUT_C sets presented in Sec. 4 is the base to automate the MCA querying algorithm. In this section, we implement the methodology presented in Sec. 4 to the topologies shown in Fig. 6, including four-eloop and five-eloop topologies. The requirements for the implementation of the MCA algorithm are presented in Table 1, including the required number of qubits and the theoretical quantum depth.

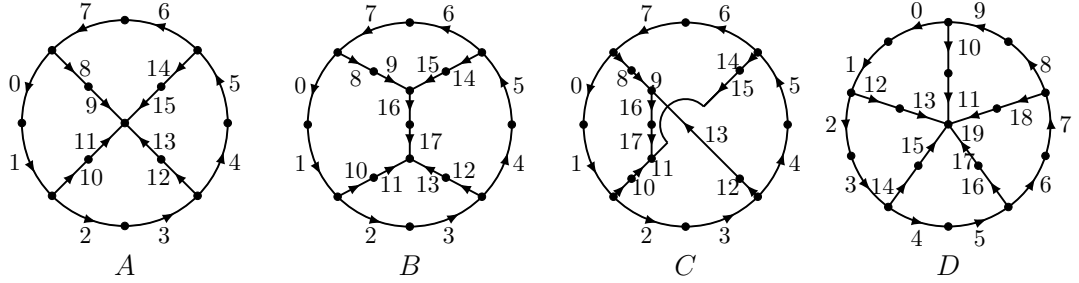


Figure 6: From left to right: four eloops with a four-point contact interaction, t - and u -channels at four eloops, and five eloops with a five-point contact interaction. Each diagram considers two edges per set.

Fig.	eloops (edges)	$ e\rangle$	$ a\rangle$	Total Qubits	Quantum Depth
6A	four ^(c) (16)	17	6	24	39
6B	four ^(t,s) (18)	18	6	26	39
6C	four ^(u) (18)	18	7	27	49
6D	five ^(c) (20)	20	9	31	57

Table 1: Quantum circuit requirements to automate the MCA quantum algorithm used to analyse the multiloop topologies in Fig. 6. The total number of qubits includes the oracle’s marker. An ancillary qubit in the $|e\rangle$ register is necessary for Fig. 6A to achieve the optimal amplitude amplification.

5.1 Four eloops with contact interaction

The four-eloop topology with a four-point contact interaction shown in Fig. 6A has DAG configurations with three, four and five sets of edges, generating a total number of twenty six eloop clauses. The number of eloop clauses is reduced to the nineteen eloop clauses shown Eq. (A.1), by fixing in $|1\rangle$ the state of e_0 . Once the eloop clauses are established, we apply the `MutualAuxMatrix` algorithm to the eloop clauses in Eq. (A.1), generating the adjacency matrix represented by the graph in Fig. 7(left).

The required number of qubits to store the eloop clauses is defined by applying the `GraphConditionCombination` algorithm to the output in the `MutualAuxMatrix` algorithm, obtaining the following sets

$$\text{MAUX}_C^{(4,16)} = \{\{c_1, c_2, c_7, \bar{c}_9\}, \{\bar{c}_1, \bar{c}_2, c_8, c_9\}, \{\bar{c}_3, \bar{c}_5, c_{10}, c_{11}\}, \{c_0, c_3, c_5\}, \{c_{12}, \bar{c}_6\}, \{c_4, c_6\}\}. \quad (5.1)$$

The output in Eq. (5.1) indicates that the number of requested ancillary qubits in the $|a\rangle$ register is six, in contrast with thirteen ancillary qubits required with the MCX algorithm [15]. This result represents a reduction of $\mathcal{O}(54\%)$ in the number of ancillary qubits.

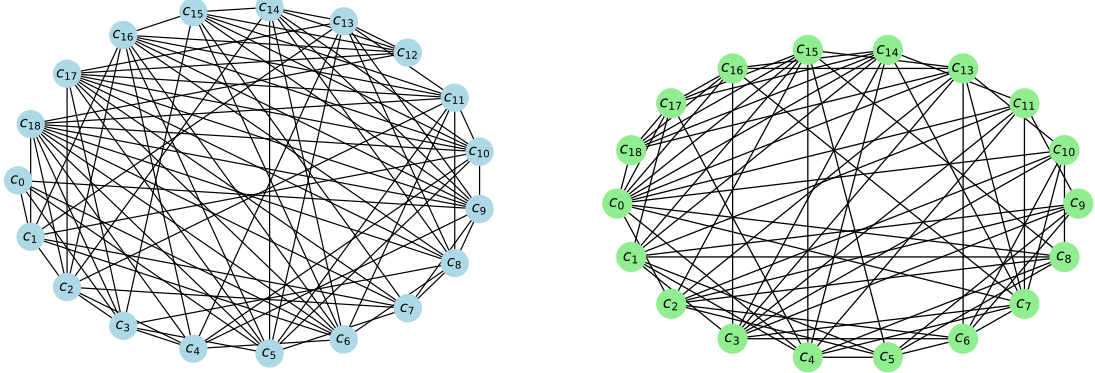


Figure 7: From left to right the graphs generated by `MutualAuxMatrix` and `MutualClausesMatrix` by using the clauses corresponding to Fig. 6A.

Regarding the implementation of eloop clauses in the quantum circuit, we start with the application of the `MutualClausesMatrix` to Eq. (A.1). The graph representation of the adjacency matrix generated is shown in Fig. 7(right). We continue with the application of the `GraphConditionCombination` algorithm to the outcome in `MutualClausesMatrix` algorithm, and then using `Optuna` we obtain

$$\text{OMUTC}^{(4,16)} = \{\{c_4, \bar{c}_2, c_0, c_7, c_{11}\}, \{c_3, c_9\}, \{c_{12}\}, \{c_6, c_2, \bar{c}_1, c_{10}\}, \{c_8, c_5, \bar{c}_3, c_1\}, \{\bar{c}_6, \bar{c}_5, \bar{c}_9\}\}. \quad (5.2)$$

The Eq. (5.2) provides the optimised clustering and ordering of the eloop clauses in the quantum circuit, and their implementation in the quantum circuit gives thirty-nine of theoretical quantum circuit depth.

5.2 The t channel at four eloops

The t –channel with two edges per set is depicted in Fig. 6B. Regarding the implementation of the algorithm, we start by fixing the state of the edge e_0 obtaining the nineteen eloop clauses shown in Eq. (A.2). Applying the algorithms `MutualAuxMatrix` and `GraphConditionCombination` in a sequential order to Eq. (A.2) we obtain

$$\text{MAUXC}^{(4,18)} = \{\{\bar{c}_7, c_8, \bar{c}_8, c_{10}, c_{11}\}, \{c_0, \bar{c}_2, \bar{c}_3, \bar{c}_4\}, \{c_6, c_9, c_{12}, \bar{c}_{12}\}, \{c_1, c_2, c_4\}, \{c_3, c_5\}, \{c_7\}\}, \quad (5.3)$$

implying the need of only six ancillary qubits in the $|a\rangle$ register. This result shows a significant reduction compared to the thirteen qubits needed in the MCX algorithm [15]. Following with the application of the algorithms `MutualClausesMatrix`, `GraphConditionCombination` and `Optuna` in a sequential order, we obtain that the optimized eloop clauses grouping is given by

$$\text{OMUTC}^{(4,18)} = \{\{c_0\}, \{c_{12}, c_{10}\}, \{c_2, c_7, c_6, c_{11}, \bar{c}_4\}, \{\bar{c}_8, c_1, \bar{c}_3, \bar{c}_{12}\}, \{\bar{c}_7\}, \{c_4, c_9, c_5, c_8, \bar{c}_2\}, \{c_3\}\}. \quad (5.4)$$

Also, the theoretical quantum circuit depth is thirty-nine.

5.3 The u -channel at four eloops

The u -channel shown in Fig. 6C considers two edges per set. The total number of eloop clauses after fixing the edge e_0 is twenty-one, shown in Eq. (A.3). Note that the complexity of the non-planar topology gives rise to four additional eloop clauses. The implementation of the MCA quantum algorithm gives that the required ancillary qubits to store the eloop clauses are given by

$$\text{MAUX}_C^{(4,18)} = \{\{c_3, \bar{c}_3, c_{10}, \bar{c}_{10}, c_{13}, \bar{c}_{13}\}, \{c_2, \bar{c}_4, \bar{c}_6, c_{11}\}, \{\bar{c}_2, c_4, \bar{c}_7, c_9\}, \{c_1, c_6, c_{12}\}, \{c_0, c_{14}\}, \{c_5, c_7\}, \{c_8\}\}, \quad (5.5)$$

and the sets optimising the eloop clauses clustering in the quantum circuit are

$$\text{OMUT}_C^{(4,18)} = \{\{c_4, c_{10}, c_{12}, c_2\}, \{c_0\}, \{c_7, \bar{c}_2, c_{11}, \bar{c}_{13}, c_8\}, \{\bar{c}_3\}, \{c_5, \bar{c}_4, c_6, c_{13}, c_9\}, \{c_3\}, \{c_1, \bar{c}_7, c_{14}, \bar{c}_6, \bar{c}_{10}\}\}. \quad (5.6)$$

In this case, the implementation of the MCA quantum algorithm needs seven ancillary qubits in the $|a\rangle$ register, representing a reduction of $\mathcal{O}(53\%)$ compared to the fifteen ancillary qubits required in the MCX algorithm [15]. The theoretical quantum circuit depth is forty-nine.

5.4 Five eloops with contact interaction

The application of the MCA quantum algorithm to the five-eloop topology considering two edges per set (Fig. 6D) provides the sets of eloop clauses associated to the ancillary qubits and the sets optimising the eloop clauses grouping in the quantum circuit implementation, explicitly

$$\text{MAUX}_C^{(5,20)} \{\{\bar{c}_6, \bar{c}_8, c_{11}, c_{14}, c_{17}\}, \{\bar{c}_1, \bar{c}_2, c_{10}, c_{16}\}, \{\bar{c}_3, \bar{c}_4, c_{12}, c_{18}\}, \{\bar{c}_7, c_8, c_{15}, c_{19}\}, \{c_1, c_2, \bar{c}_{11}, c_{13}\}, \{c_3, c_6, c_9, \bar{c}_{12}\}, \{c_4, c_5, c_7, \bar{c}_{16}\}, \{c_0\}, \{c_{20}\}\}, \quad (5.7)$$

and

$$\text{OMUT}_C^{(5,20)} = \{\{c_{17}, c_3, \bar{c}_1, c_{12}, c_8, c_7, c_{13}\}, \{\bar{c}_6, \bar{c}_{11}, \bar{c}_{16}, \bar{c}_{12}, \bar{c}_7, \bar{c}_2\}, \{c_9, c_{14}, c_{19}, c_0, c_5, \bar{c}_3, c_{10}\}, \{\bar{c}_8\}, \{\bar{c}_4, c_6, c_{15}, c_1, c_{11}\}, \{c_{16}, c_2, c_4\}, \{c_{20}\}, \{c_{18}\}\}. \quad (5.8)$$

Based on Eq. (5.7), we assign nine ancillary qubits to store the eloop clauses in the MCA quantum algorithm, whereas the MCX quantum algorithm needs twenty-one. This comparison represents a reduction of $\mathcal{O}(57\%)$. Additionally, the theoretical quantum circuit depth is fifty-seven.

In this section, we have shown a significant reduction in the total number of qubits needed to implement the MCA quantum algorithm compared with the MCX quantum algorithm [15]. In Table 2 we provide a summary of the number of qubits needed for an

eloops	MCA $ a\rangle$	MCX $ a\rangle$	Gain in $ a\rangle$
three	2 to 3	4 to 7	$\mathcal{O}(50\%)$ to $\mathcal{O}(57\%)$
four ^(c,t)	4 to 6	5 to 13	$\mathcal{O}(20\%)$ to $\mathcal{O}(61\%)$
four ^(u)	4 to 7	5 to 15	$\mathcal{O}(20\%)$ to $\mathcal{O}(53\%)$
five ^(c)	5 to 9	6 to 21	$\mathcal{O}(16\%)$ to $\mathcal{O}(57\%)$

Table 2: Number of qubits required to implement the eloop clauses for the MCA quantum algorithm proposed in this work, and the MCX quantum algorithm from Ref. [15] for an arbitrary three-, four- and five-eloop configuration. The minimum number of qubits in the $|a\rangle$ register occurs when there is only one edge in each set, the maximum number is saturated when all sets contain at least two edges.

arbitrary three-, four- and five-eloop topology. Furthermore, the idea of mutually exclusive clauses was also applied to automate the construction of the oracle, defining a proper order in the application of the quantum gates.

6 Transpilation behaviour

The success of the MCA quantum algorithm in reducing the number of ancillary qubits is due to the fact that the complexity of the analysed topologies requires the maximum number of eloop clauses. To illustrate this comment, we apply both algorithms to a three-eloop topology with nine and twelve edges, and a four-eloop topology with twelve and sixteen edges. Regarding the required number of qubits, the third and fourth columns in Table 3 exhibits a wider range of improvement in topologies with higher complexity, which is an advantage to explore more complex topologies. In terms of the theoretical quantum circuit depth [60], the fifth column in Table 3 shows a similar behaviour than the third and fourth columns, having a wider range of improvement in the more complex topologies.

Beyond the theoretical quantum circuit depth, we are interested in analysing the effect of transpilation, the process of compiling a given quantum circuit to match the specific

eloops (edges)	$ e\rangle$	$ a\rangle$	Total Qubits	Quantum Depth	Total states
three (9)	9	2 4	12 14	15 17	512
three (12)	12	3 7	16 21	23 31	8192
four ^(c) (12)	12	4 5	17 18	15 15	4096
four ^(c) (16)	17	6 13	24 31	39 45	131072

Table 3: Quantum resources required and theoretical quantum circuit depth of the quantum algorithms used to analyse the three-eloop topology with nine and twelve edges, and the four-eloop topology with twelve and sixteen edges. The first number in the third, fourth and fifth columns are from the MCA quantum algorithm, whereas the second number corresponds to MCX quantum algorithm.

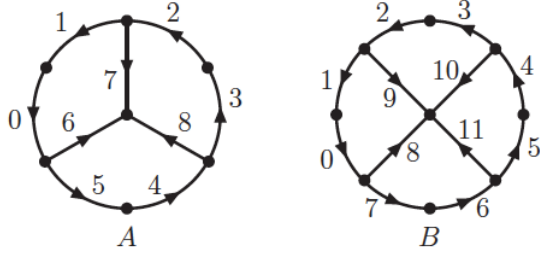


Figure 8: Three-eloop topology with nine edges (left), and four eloops with a four-point contact interaction and twelve edges (right).

topology and native gate set of a particular quantum device hardware, as well as optimising it to run on Noisy Intermediate Scale Quantum (NISQ) era computers. In order to analyse the impact of transpilation, it is important to take into account that this process may involve more qubits than those needed in the quantum circuit design. Therefore, in addition to the transpiled quantum circuit depth, we incorporate the quantum circuit area [15] in the study. This metric is defined as the product of the transpiled quantum circuit depth and the number of qubits required in the transpilation, which provides a better perspective on the computational complexity of the quantum circuit. The transpilation process is executed for relevant metrics in the available quantum backends, `ibm_brisbane`, both simulated and real using the Qiskit framework to analize and compare the behaviour through different optimization levels, from one to three.

The aim of the optimizations levels is to minimize the depth of the quantum circuit by reducing the noise and errors introduced by the hardware used, mainly by adapting to the topology of the quantum circuit. The optimization levels in Qiskit [61] are classified as 0, 1, 2 and 3. The differences between levels 1, 2 and 3 are mainly based on the application of different gate simplification algorithms and an increase in the number of their iterations

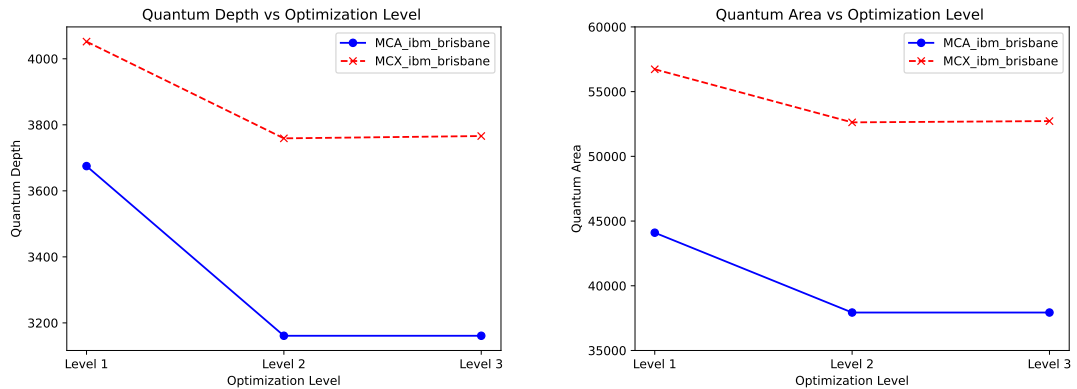


Figure 9: Quantum circuit depth (left) and quantum cicut area (right) for the three-eloop topology with nine edges (Fig. 8A) implementing the MCX and MCA quantum algorithms for different optimisation levels.

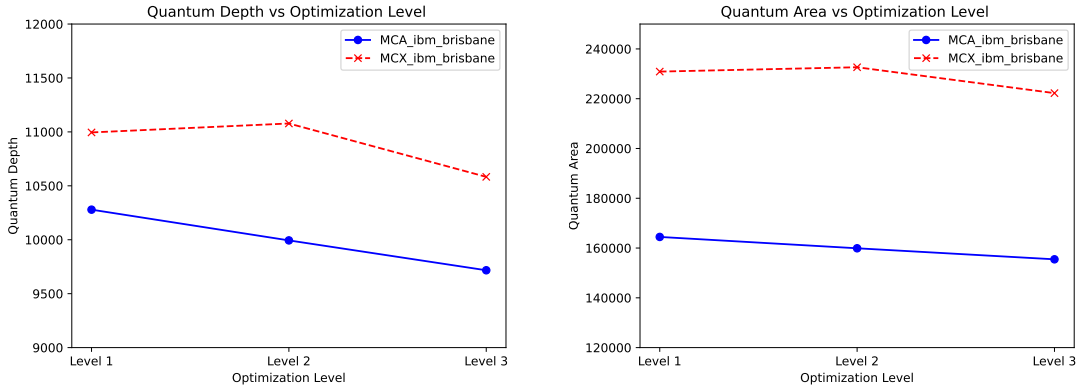


Figure 10: Quantum circuit depth (left) and quantum circuit area (right) for the three-eloop topology with twelve edges (Fig. 1) implementing the MCX and MCA quantum algorithms for different optimisation levels.

used to find the best configuration. The process changes in the case of level zero, the Qiskit algorithm only tries to use the same number of virtual qubits as physical qubits and uses swap gates to correct the physical qubit connections caused by the hardware topology. The use of swap gates increases the quantum depth of the circuit enormously, even taking into account the transpilation of the gates used in the circuit. Regarding the remaining levels, they apply the same steps as in level 0 and include a new method called `VF2LayoutPostLayout` [62]. This method transforms the quantum circuit and the hardware into graphs, with the aim of identifying isomorphisms between them. The `VF2LayoutPostLayout` method creates a dependency on the type of hardware used, and therefore the same quantum algorithm can have a worse or better use of the physical qubits and of the quantum depth, depending on the topology of the hardware used.

We continue the analysis with the three-eloop topology with nine edges (Fig. 8A). Despite the fact that no significant difference was observed in terms of the theoretical quantum circuit depth, the MCA quantum algorithm exhibits a better performance than the MCX quantum algorithm in terms of the transpiled quantum circuit depth and quantum circuit area, as shown in Fig. 9. In the case of the three-eloop topology with twelve edges (Fig. 1), according to Fig. 10, the MCA quantum algorithm also exhibits a better performance than the MCX quantum algorithm in terms of the transpiled quantum circuit depth and the quantum circuit area.

Moving forward to the four-eloop topology with twelve edges, the transpiled quantum circuit depth and the quantum circuit area shown in Fig. 11, shows again a favourable result for the MCA quantum algorithm. In the case of the four-eloop topology with sixteen edges, we observe in Fig. 12 less transpiled quantum circuit depth with the MCA quantum algorithm. Regarding the quantum circuit area, we observe that the MCA quantum algorithm outperforms MCX, which is expected due to the reduction of qubits and theoretical quantum depth.

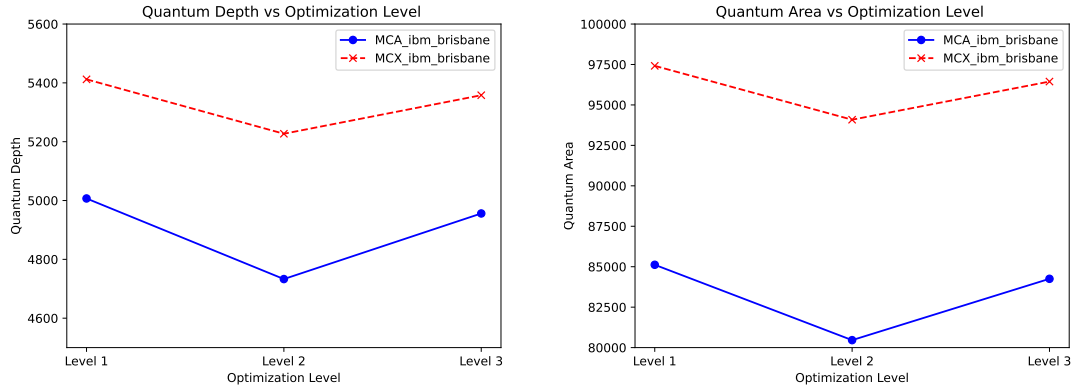


Figure 11: Quantum circuit depth (left) and quantum circuit area (right) for the four-eloop topology with twelve edges (Fig. 8B) for the MCX and MCA quantum algorithms for different optimisation levels.

From the analysis of the transpilation behaviour between the MCA and MCX algorithms, we have shown a significantly better performance of the MCA quantum algorithm in terms of the transpiled quantum circuit depth and the quantum area. The transpiled quantum circuit depth of the MCA quantum algorithm presents a reduction of at least $\mathcal{O}(10\%)$ compared to the MCX quantum algorithm, and an improvement of at least $\mathcal{O}(15\%)$ in terms of the quantum area.

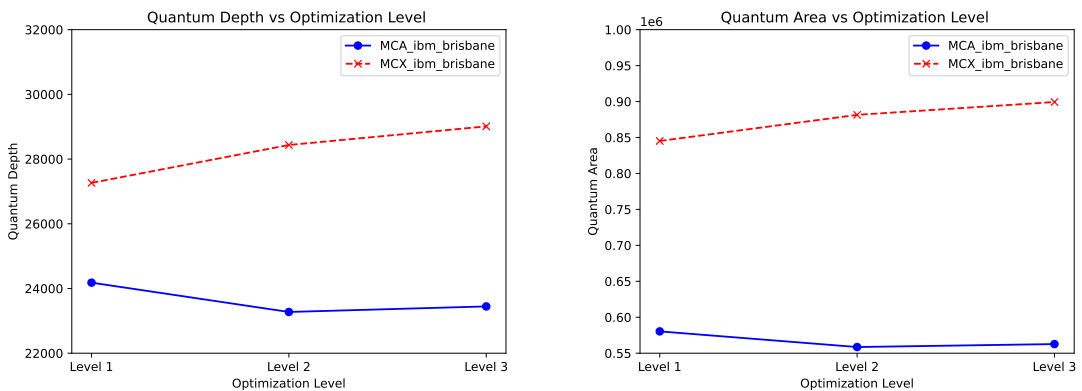


Figure 12: Quantum circuit depth (left) and quantum circuit area (right) for the four-eloop topology with sixteen edges (Fig. 6A) for the MCX and MCA quantum algorithms for different optimisation levels.

7 Conclusions

We have presented an automated query quantum algorithm, the Minimum Clique-optimised quantum Algorithm (MCA), for the identification of DAG configurations of multiloop graphs, which is equivalent to determining the causal configurations of multiloop Feynman diagrams in particle physics. This approach introduces an automated method for oracle design by leveraging the MCP problem from graph theory in combination with hyperparameter optimization techniques. The MCA quantum algorithm optimizes both the required number of ancillary qubits and the theoretical quantum circuit depth. It has been implemented on three-, four-, and five-eloop topologies, successfully identifying the corresponding DAG or causal configurations in each case. The results demonstrate a significant reduction in the number of ancillary qubits required for more complex topologies when using the MCA algorithm, compared to the MCX quantum algorithm. Furthermore, by applying the same principles to minimize ancillary qubit usage and utilizing the Optuna framework for hyperparameter optimization, we also achieved a considerable reduction in the theoretical quantum circuit depth.

We also evaluated the performance of quantum circuits generated by the MCA algorithm after transpilation for execution on real quantum hardware. Notably, the MCA algorithm demonstrated substantial improvements in quantum metrics, specifically in terms of reduced quantum circuit depth and smaller quantum circuit area. These results highlight the enhanced performance and resource efficiency of the MCA approach over the MCX quantum algorithm.

Acknowledgements

This work is supported by the Mexican Government - Secretaría de Ciencia, Humanidades, Tecnología e Innovación (SECIHTI), Grants No. CBF2023-2024-268 and No. CBF2023-2024-3544 and *Sistema Nacional de Investigadores*; the Spanish Government and ERDF/EU - Agencia Estatal de Investigación (MCIU/AEI/10.13039/501100011033), Grants No. PID2023-146220NB-I00, No. PID2020-114473GB-I00, and No. CEX2023-001292-S; and Generalitat Valenciana, Grant No. ASFAE/2022/009 (Planes Complementarios de I+D+i, NextGenerationEU). This work is also supported by the Ministry of Economic Affairs and Digital Transformation of the Spanish Government and NextGenerationEU through the Quantum Spain project, and by CSIC Interdisciplinary Thematic Platform (PTI+) on Quantum Technologies (PTI-QTEP+). In addition, the work that led to these results received the support from the “la Caixa” Foundation (ID 100010434) fellowship code is LCF/BQ/DFI25/130000.

References

- [1] CMS collaboration, S. Chatrchyan et al., *Observation of a New Boson at a Mass of 125 GeV with the CMS Experiment at the LHC*, *Phys. Lett. B* **716** (2012) 30–61, [[1207.7235](#)].
- [2] ATLAS collaboration, G. Aad et al., *Observation of a new particle in the search for the Standard Model Higgs boson with the ATLAS detector at the LHC*, *Phys. Lett. B* **716** (2012) 1–29, [[1207.7214](#)].
- [3] LINEAR COLLIDER VISION collaboration, D. Attié et al., *A Linear Collider Vision for the Future of Particle Physics*, [2503.19983](#).
- [4] CLIC, CLICDP collaboration, P. Roloff, R. Franceschini, U. Schnoor and A. Wulzer, *The Compact Linear e^+e^- Collider (CLIC): Physics Potential*, [1812.07986](#).
- [5] ILC collaboration, G. Aarons et al., *International Linear Collider Reference Design Report Volume 2: Physics at the ILC*, [0709.1893](#).
- [6] CEPC STUDY GROUP collaboration, M. Dong et al., *CEPC Conceptual Design Report: Volume 2 - Physics & Detector*, [1811.10545](#).
- [7] FCC collaboration, M. Benedikt et al., *Future Circular Collider Feasibility Study Report: Volume 1, Physics, Experiments, Detectors*, [2505.00272](#).
- [8] FCC collaboration, A. Abada et al., *FCC Physics Opportunities: Future Circular Collider Conceptual Design Report Volume 1*, *Eur. Phys. J. C* **79** (2019) 474.
- [9] G. Heinrich, *Collider Physics at the Precision Frontier*, *Phys. Rept.* **922** (2021) 1–69, [[2009.00516](#)].
- [10] A. Di Meglio et al., *Quantum Computing for High-Energy Physics: State of the Art and Challenges*, *PRX Quantum* **5** (2024) 037001, [[2307.03236](#)].
- [11] A. Delgado et al., *Quantum Computing for Data Analysis in High-Energy Physics*, in *Snowmass 2021*, 3, 2022. [2203.08805](#).
- [12] G. Rodrigo, *Quantum Algorithms in Particle Physics*, *Acta Phys. Polon. Supp.* **17** (2024) 2–A14, [[2401.16208](#)].
- [13] S. Ramírez-Uribe, A. E. Rentería-Olivo, G. Rodrigo, G. F. R. Sborlini and L. Vale Silva, *Quantum algorithm for Feynman loop integrals*, *JHEP* **05** (2022) 100, [[2105.08703](#)].
- [14] G. Clemente, A. Crippa, K. Jansen, S. Ramírez-Uribe, A. E. Rentería-Olivo, G. Rodrigo et al., *Variational quantum eigensolver for causal loop Feynman diagrams and directed acyclic graphs*, *Phys. Rev. D* **108** (2023) 096035, [[2210.13240](#)].
- [15] S. Ramírez-Uribe, A. E. Rentería-Olivo and G. Rodrigo, *Quantum querying based on multicontrolled Toffoli gates for causal Feynman loop configurations and directed acyclic graphs*, [2404.03544](#).
- [16] J. J. Aguilera-Verdugo, R. J. Hernandez-Pinto, G. Rodrigo, G. F. R. Sborlini and W. J. Torres Bobadilla, *Causal representation of multi-loop Feynman integrands within the loop-tree duality*, *JHEP* **01** (2021) 069, [[2006.11217](#)].

[17] S. Ramírez-Uribe, R. J. Hernández-Pinto, G. Rodrigo, G. F. R. Sborlini and W. J. Torres Bobadilla, *Universal opening of four-loop scattering amplitudes to trees*, *JHEP* **04** (2021) 129, [[2006.13818](#)].

[18] S. Ramírez-Uribe, P. K. Dhani, G. F. R. Sborlini and G. Rodrigo, *Rewriting Theoretical Predictions at Colliders with Vacuum Amplitudes*, *Phys. Rev. Lett.* **133** (2024) 211901, [[2404.05491](#)].

[19] LTD collaboration, S. Ramírez-Uribe, A. E. Rentería-Olivo, D. F. Rentería-Estrada, J. J. M. de Lejarza, P. K. Dhani, L. Cieri et al., *Vacuum amplitudes and time-like causal unitarity in the loop-tree duality*, *JHEP* **01** (2025) 103, [[2404.05492](#)].

[20] A. Dumitrescu and J. Pach, *Minimum clique partition in unit disk graphs*, *Graphs and Combinatorics* **27** (2011) 399–411.

[21] S. Catani, T. Gleisberg, F. Krauss, G. Rodrigo and J.-C. Winter, *From loops to trees by-passing Feynman’s theorem*, *JHEP* **09** (2008) 065, [[0804.3170](#)].

[22] I. Bierenbaum, S. Catani, P. Draggiotis and G. Rodrigo, *A Tree-Loop Duality Relation at Two Loops and Beyond*, *JHEP* **10** (2010) 073, [[1007.0194](#)].

[23] I. Bierenbaum, S. Buchta, P. Draggiotis, I. Malamos and G. Rodrigo, *Tree-Loop Duality Relation beyond simple poles*, *JHEP* **03** (2013) 025, [[1211.5048](#)].

[24] S. Buchta, G. Chachamis, P. Draggiotis, I. Malamos and G. Rodrigo, *On the singular behaviour of scattering amplitudes in quantum field theory*, *JHEP* **11** (2014) 014, [[1405.7850](#)].

[25] S. Buchta, G. Chachamis, P. Draggiotis and G. Rodrigo, *Numerical implementation of the loop-tree duality method*, *Eur. Phys. J. C* **77** (2017) 274, [[1510.00187](#)].

[26] R. J. Hernandez-Pinto, G. F. R. Sborlini and G. Rodrigo, *Towards gauge theories in four dimensions*, *JHEP* **02** (2016) 044, [[1506.04617](#)].

[27] G. F. R. Sborlini, F. Driencourt-Mangin, R. Hernandez-Pinto and G. Rodrigo, *Four-dimensional unsubtraction from the loop-tree duality*, *JHEP* **08** (2016) 160, [[1604.06699](#)].

[28] G. F. R. Sborlini, F. Driencourt-Mangin and G. Rodrigo, *Four-dimensional unsubtraction with massive particles*, *JHEP* **10** (2016) 162, [[1608.01584](#)].

[29] E. T. Tomboulis, *Causality and Unitarity via the Tree-Loop Duality Relation*, *JHEP* **05** (2017) 148, [[1701.07052](#)].

[30] F. Driencourt-Mangin, G. Rodrigo and G. F. R. Sborlini, *Universal dual amplitudes and asymptotic expansions for $gg \rightarrow H$ and $H \rightarrow \gamma\gamma$ in four dimensions*, *Eur. Phys. J. C* **78** (2018) 231, [[1702.07581](#)].

[31] J. L. Jurado, G. Rodrigo and W. J. Torres Bobadilla, *From Jacobi off-shell currents to integral relations*, *JHEP* **12** (2017) 122, [[1710.11010](#)].

[32] F. Driencourt-Mangin, G. Rodrigo, G. F. R. Sborlini and W. J. Torres Bobadilla, *Universal*

four-dimensional representation of $H \rightarrow \gamma\gamma$ at two loops through the Loop-Tree Duality, *JHEP* **02** (2019) 143, [[1901.09853](#)].

[33] R. Runkel, Z. Szőr, J. P. Vesga and S. Weinzierl, *Causality and loop-tree duality at higher loops*, *Phys. Rev. Lett.* **122** (2019) 111603, [[1902.02135](#)].

[34] J. J. Aguilera-Verdugo, F. Driencourt-Mangin, J. Plenter, S. Ramírez-Uribe, G. Rodrigo, G. F. R. Sborlini et al., *Causality, unitarity thresholds, anomalous thresholds and infrared singularities from the loop-tree duality at higher orders*, *JHEP* **12** (2019) 163, [[1904.08389](#)].

[35] R. Runkel, Z. Szőr, J. P. Vesga and S. Weinzierl, *Integrands of loop amplitudes within loop-tree duality*, *Phys. Rev. D* **101** (2020) 116014, [[1906.02218](#)].

[36] Z. Capatti, V. Hirschi, D. Kermanschah and B. Ruijl, *Loop-Tree Duality for Multiloop Numerical Integration*, *Phys. Rev. Lett.* **123** (2019) 151602, [[1906.06138](#)].

[37] F. Driencourt-Mangin, G. Rodrigo, G. F. R. Sborlini and W. J. Torres Bobadilla, *Interplay between the loop-tree duality and helicity amplitudes*, *Phys. Rev. D* **105** (2022) 016012, [[1911.11125](#)].

[38] Z. Capatti, V. Hirschi, D. Kermanschah, A. Pelloni and B. Ruijl, *Numerical Loop-Tree Duality: contour deformation and subtraction*, *JHEP* **04** (2020) 096, [[1912.09291](#)].

[39] J. Plenter and G. Rodrigo, *Asymptotic expansions through the loop-tree duality*, *Eur. Phys. J. C* **81** (2021) 320, [[2005.02119](#)].

[40] R. M. Prisco and F. Tramontano, *Dual subtractions*, *JHEP* **06** (2021) 089, [[2012.05012](#)].

[41] J. J. Aguilera-Verdugo, F. Driencourt-Mangin, R. J. Hernández-Pinto, J. Plenter, S. Ramírez-Uribe, A. E. Rentería Olivo et al., *Open Loop Amplitudes and Causality to All Orders and Powers from the Loop-Tree Duality*, *Phys. Rev. Lett.* **124** (2020) 211602, [[2001.03564](#)].

[42] J. J. Aguilera-Verdugo, R. J. Hernández-Pinto, S. Ramírez-Uribe, A. E. Rentería-Olivo, G. Rodrigo, G. F. R. Sborlini et al., *Manifestly Causal Scattering Amplitudes*, [https://www.snowmass21.org/docs/files/summaries/TF/SNOWMASS21-
TF4_TF6_TorresBobadilla-093.pdf](https://www.snowmass21.org/docs/files/summaries/TF/SNOWMASS21-TF4_TF6_TorresBobadilla-093.pdf), *Snowmass LoI* (August 2020) .

[43] J. Jesús Aguilera-Verdugo, R. J. Hernández-Pinto, G. Rodrigo, G. F. R. Sborlini and W. J. Torres Bobadilla, *Mathematical properties of nested residues and their application to multi-loop scattering amplitudes*, *JHEP* **02** (2021) 112, [[2010.12971](#)].

[44] G. F. R. Sborlini, *Geometrical approach to causality in multiloop amplitudes*, *Phys. Rev. D* **104** (2021) 036014, [[2102.05062](#)].

[45] W. J. Torres Bobadilla, *Loop-tree duality from vertices and edges*, *JHEP* **04** (2021) 183, [[2102.05048](#)].

[46] W. J. T. Bobadilla, *Lotty – The loop-tree duality automation*, *Eur. Phys. J. C* **81** (2021) 514, [[2103.09237](#)].

[47] J. de Jesús Aguilera-Verdugo et al., *A Stroll through the Loop-Tree Duality*, *Symmetry* **13** (2021) 1029, [[2104.14621](#)].

[48] J. Rios-Sánchez and G. Sborlini, *Toward multiloop local renormalization within causal loop-tree duality*, *Phys. Rev. D* **109** (2024) 125004, [[2402.13995](#)].

[49] I. L. Imaz and G. F. R. Sborlini, *Analysis of symmetries in the causal loop-tree duality representations*, *Phys. Rev. D* **111** (2025) 105016, [[2502.14179](#)].

[50] L. K. Grover, *Quantum mechanics helps in searching for a needle in a haystack*, *Phys. Rev. Lett.* **79** (1997) 325–328, [[quant-ph/9706033](#)].

[51] S. Ramírez-Uribe, R. J. Hernández-Pinto, G. Rodrigo and G. F. R. Sborlini, *From Five-Loop Scattering Amplitudes to Open Trees with the Loop-Tree Duality*, *Symmetry* **14** (2022) 2571, [[2211.03163](#)].

[52] V. Bergholm et al., *PennyLane: Automatic differentiation of hybrid quantum-classical computations*, [1811.04968](#).

[53] B. R. Preiss, *Data Structures and Algorithms*. John Wiley & Sons, Inc., USA, 1st ed., 1999.

[54] F. Riaz and K. M. Ali, *Applications of graph theory in computer science*, in *2011 Third International Conference on Computational Intelligence, Communication Systems and Networks*, pp. 142–145, 2011. [DOI](#).

[55] R. M. Karp, *Reducibility Among Combinatorial Problems*, pp. 219–241. Springer Berlin Heidelberg, Berlin, Heidelberg, 2010. 10.1007/978-3-540-68279-0_8.

[56] A. Hagberg, P. J. Swart and D. A. Schult, *Exploring network structure, dynamics, and function using networkx*, tech. rep., Los Alamos National Laboratory (LANL), Los Alamos, NM (United States), 2008.

[57] C. Bron and J. Kerbosch, *Algorithm 457: finding all cliques of an undirected graph*, *Commun. ACM* **16** (Sept., 1973) 575–577.

[58] T. Akiba, S. Sano, T. Yanase, T. Ohta and M. Koyama, *Optuna: A next-generation hyperparameter optimization framework*, in *Proceedings of the 25th ACM SIGKDD international conference on knowledge discovery & data mining*, pp. 2623–2631, 2019. [1907.10902](#). [DOI](#).

[59] S. Watanabe, *Tree-structured parzen estimator: Understanding its algorithm components and their roles for better empirical performance*, [2304.11127](#).

[60] Quantum Computing Stack Exchange, *How to calculate circuit depth properly?*, <https://quantumcomputing.stackexchange.com/questions/5769/how-to-calculate-circuit-depth-properly>, 2020.

[61] IBM Quantum, *Set optimization*, 2024.

[62] Qiskit Development Team, *Vf2postlayout — qiskit documentation*, 2024.

A Clauses of multiloop topologies: four and five eloops

A.1 Four eloops with contact interaction

The corresponding eloop clauses for the four-eloop topology shown in Fig. 6A are

$$\begin{aligned}
c_0 &= s_0 \wedge \bar{s}_4 \wedge s_5 , & c_1 &= s_1 \wedge \bar{s}_5 \wedge s_6 , \\
c_2 &= s_2 \wedge \bar{s}_6 \wedge s_7 , & c_3 &= s_3 \wedge s_4 \wedge \bar{s}_7 , \\
c_4 &= s_0 \wedge s_1 \wedge \bar{s}_4 \wedge s_6 , & c_5 &= s_1 \wedge s_2 \wedge \bar{s}_5 \wedge s_7 , \\
c_6 &= s_2 \wedge s_3 \wedge s_4 \wedge \bar{s}_6 , & c_7 &= s_0 \wedge s_3 \wedge s_5 \wedge \bar{s}_7 , \\
c_8 &= s_0 \wedge s_1 \wedge s_2 \wedge \bar{s}_4 \wedge s_7 , & c_9 &= s_1 \wedge s_2 \wedge s_3 \wedge s_4 \wedge \bar{s}_5 , \\
c_{10} &= s_0 \wedge s_2 \wedge s_3 \wedge s_5 \wedge \bar{s}_6 , & c_{11} &= s_0 \wedge s_1 \wedge s_3 \wedge s_6 \wedge \bar{s}_7 , \\
c_{12} &= s_0 \wedge s_1 \wedge s_2 \wedge s_3 & c_{13} &= \bar{c}_1 , \quad c_{14} = \bar{c}_2 , \\
c_{15} &= \bar{c}_3 , \quad c_{16} = \bar{c}_5 , & c_{17} &= \bar{c}_6 , \quad c_{18} = \bar{c}_9 .
\end{aligned} \tag{A.1}$$

A.2 Four eloops: s – and t –channels

The corresponding eloop clauses for the t -channel with two edges per set shown in Fig. 6B are

$$\begin{aligned}
c_0 &= s_0 \wedge s_1 \wedge s_2 \wedge s_3 , & c_1 &= s_0 \wedge \bar{s}_4 \wedge s_5 , \\
c_2 &= s_1 \wedge \bar{s}_5 \wedge s_6 \wedge s_8 , & c_3 &= s_2 \wedge \bar{s}_6 \wedge s_7 , \\
c_4 &= s_3 \wedge s_4 \wedge \bar{s}_7 \wedge \bar{s}_8 , & c_5 &= s_0 \wedge s_3 \wedge s_5 \wedge \bar{s}_7 \wedge \bar{s}_8 , \\
c_6 &= s_0 \wedge s_1 \wedge \bar{s}_4 \wedge s_6 \wedge s_8 , & c_7 &= s_1 \wedge s_2 \wedge \bar{s}_5 \wedge s_7 \wedge s_8 , \\
c_8 &= s_2 \wedge s_3 \wedge s_4 \wedge \bar{s}_6 \wedge \bar{s}_8 , & c_9 &= s_0 \wedge s_2 \wedge s_3 \wedge s_5 \wedge \bar{s}_6 \wedge \bar{s}_8 , \\
c_{10} &= s_0 \wedge s_1 \wedge s_3 \wedge s_6 \wedge \bar{s}_7 , & c_{11} &= s_0 \wedge s_1 \wedge s_2 \wedge \bar{s}_4 \wedge s_7 \wedge s_8 , \\
c_{12} &= s_1 \wedge s_2 \wedge s_3 \wedge s_4 \wedge \bar{s}_5 , & c_{13} &= \bar{c}_2 , \quad c_{14} = \bar{c}_3 , \\
c_{15} &= \bar{c}_4 , \quad c_{16} = \bar{c}_7 , & c_{17} &= \bar{c}_8 , \quad c_{18} = \bar{c}_{12} .
\end{aligned} \tag{A.2}$$

The eloop clauses for the so-called s -channel [17] correspond to a proper rotation and relabeling of the sets of edges.

A.3 Four eloops: u channel

The corresponding eloop clauses for the u -channel with two edges per set shown in Fig. 6C are

$$\begin{aligned}
c_0 &= s_0 \wedge s_1 \wedge s_2 \wedge s_3, & c_1 &= s_0 \wedge \bar{s}_4 \wedge s_5 \wedge \bar{s}_8, \\
c_2 &= s_1 \wedge \bar{s}_5 \wedge s_6 \wedge s_8, & c_3 &= s_2 \wedge \bar{s}_6 \wedge s_7 \wedge \bar{s}_8, \\
c_4 &= s_3 \wedge s_4 \wedge \bar{s}_7 \wedge s_8, & c_5 &= s_0 \wedge s_1 \wedge \bar{s}_4 \wedge s_6, \\
c_6 &= s_1 \wedge s_2 \wedge \bar{s}_5 \wedge s_7, & c_7 &= s_2 \wedge s_3 \wedge s_4 \wedge \bar{s}_6, \\
c_8 &= s_0 \wedge s_3 \wedge s_5 \wedge \bar{s}_7, & c_9 &= s_0 \wedge s_1 \wedge s_2 \wedge \bar{s}_4 \wedge s_7 \wedge \bar{s}_8, \\
c_{10} &= s_1 \wedge s_2 \wedge s_3 \wedge s_4 \wedge \bar{s}_5 \wedge s_8, & c_{11} &= s_0 \wedge s_2 \wedge s_3 \wedge s_5 \wedge \bar{s}_6 \wedge \bar{s}_8, \\
c_{12} &= s_0 \wedge s_1 \wedge s_3 \wedge s_6 \wedge \bar{s}_7 \wedge s_8, & c_{13} &= s_1 \wedge \bar{s}_3 \wedge \bar{s}_4 \wedge \bar{s}_5 \wedge s_6 \wedge s_7, \\
c_{14} &= s_0 \wedge \bar{s}_2 \wedge \bar{s}_4 \wedge s_5 \wedge s_6 \wedge \bar{s}_7, & c_{15} &= \bar{c}_2, \quad c_{16} = \bar{c}_3, \quad c_{17} = \bar{c}_4, \\
c_{18} &= \bar{c}_6, \quad c_{19} = \bar{c}_7, \quad c_{20} = \bar{c}_{10}, \quad c_{21} = \bar{c}_{13}.
\end{aligned} \tag{A.3}$$

A.4 Five eloops with contact interaction

The corresponding eloop clauses for the five-eloop topology with two edges per set shown in Fig. 6D are

$$\begin{aligned}
c_0 &= s_0 \wedge \bar{s}_5 \wedge s_6, & c_1 &= s_1 \wedge \bar{s}_6 \wedge s_7, \\
c_2 &= s_2 \wedge \bar{s}_7 \wedge s_8, & c_3 &= s_3 \wedge \bar{s}_8 \wedge s_9, \\
c_4 &= s_4 \wedge s_5 \wedge \bar{s}_9, & c_5 &= s_0 \wedge s_1 \wedge \bar{s}_5 \wedge s_7, \\
c_6 &= s_1 \wedge s_2 \wedge \bar{s}_6 \wedge s_8, & c_7 &= s_2 \wedge s_3 \wedge \bar{s}_7 \wedge s_9, \\
c_8 &= s_3 \wedge s_4 \wedge s_5 \wedge \bar{s}_8, & c_9 &= s_0 \wedge s_4 \wedge s_6 \wedge \bar{s}_9, \\
c_{10} &= s_0 \wedge s_1 \wedge s_2 \wedge \bar{s}_5 \wedge s_8, & c_{11} &= s_1 \wedge s_2 \wedge s_3 \wedge \bar{s}_6 \wedge s_9, \\
c_{12} &= s_2 \wedge s_3 \wedge s_4 \wedge s_5 \wedge \bar{s}_7, & c_{13} &= s_0 \wedge s_3 \wedge s_4 \wedge s_6 \wedge \bar{s}_8, \\
c_{14} &= s_0 \wedge s_1 \wedge s_4 \wedge s_7 \wedge \bar{s}_9, & c_{15} &= s_0 \wedge s_1 \wedge s_2 \wedge s_3 \wedge \bar{s}_5 \wedge s_9, \\
c_{16} &= s_1 \wedge s_2 \wedge s_3 \wedge s_4 \wedge s_5 \wedge \bar{s}_6, & c_{17} &= s_0 \wedge s_2 \wedge s_3 \wedge s_4 \wedge s_6 \wedge \bar{s}_7, \\
c_{18} &= s_0 \wedge s_1 \wedge s_3 \wedge s_4 \wedge s_7 \wedge \bar{s}_8, & c_{19} &= s_0 \wedge s_1 \wedge s_2 \wedge s_4 \wedge s_8 \wedge \bar{s}_9, \\
c_{20} &= s_0 \wedge s_1 \wedge s_2 \wedge s_3 \wedge s_4, & c_{21} &= \bar{c}_1, \quad c_{22} = \bar{c}_2, \\
c_{23} &= \bar{c}_3, \quad c_{24} = \bar{c}_4, & c_{25} &= \bar{c}_6, \quad c_{26} = \bar{c}_7, \\
c_{27} &= \bar{c}_8, \quad c_{28} = \bar{c}_{11}, & c_{29} &= \bar{c}_{12}, \quad c_{30} = \bar{c}_{16}.
\end{aligned} \tag{A.4}$$

B Algorithms

The **Algorithm 1** generates an adjacency matrix called `MutualAuxMatrix`. The entries of the matrix are established by the condition in Eq. (4.2), one if the pair of clauses satisfies the condition and zero if not.

Algorithm 1 `MutualAuxMatrix`

```
1: Input:  $c_1, c_2, \dots, c_n$  # All clauses
2: Output: aux_matrix #  $n \times n$  matrix
3: num_clauses  $\leftarrow n$ 
4: aux_matrix  $\leftarrow$  empty matrix of size  $n \times n$ 
5: for  $i = 1$  to num_clauses do
6:   for  $j = i$  to num_clauses do
7:     if  $c_i \vee c_j = c_i \vee c_j$  then
8:       aux_matrix[ $i, j$ ]  $\leftarrow 1$ 
9:     else
10:      aux_matrix[ $i, j$ ]  $\leftarrow 0$ 
11:    end if
12:   end for
13: end for
14: return aux_matrix
```

The **Algorithm 2**, called `GraphConditionCombination`, obtains the minimum number of cliques in a graph. The algorithm uses the function `find_cliques`² from `Networkx` library [57] which obtains all cliques in the provided adjacency matrix.

Algorithm 2 `GraphConditionCombination`

```
1: Input: conditional_graph # A graph where we search for combinations based
   on a condition
2: Output: clauses_combination # A list of maximal subgroups of cliques in the
   graph
3: clauses_combination  $\leftarrow$  empty list
4: while conditional_graph has nodes do
5:   max_clique  $\leftarrow$  the largest clique in conditional_graph
6:   append max_clique to clauses_combination
7:   remove nodes in max_clique from conditional_graph
8: end while
9: return clauses_combination
```

²This function is based on the algorithm described in Ref. [56]